Supplemental Information

Supplemental methods

Remote sensing vegetation characteristics, including forest structural variability

Vegetation characteristics can be measured using remotely-sensed imagery (Rouse *et al.* 1973; Asner *et al.* 2016; Young *et al.* 2017) and texture analysis of this imagery can quantify ecologically relevant local environmental heterogeneity across broad spatial extents (Wood *et al.* 2012; Huang *et al.* 2014; Stein *et al.* 2014; Tuanmu & Jetz 2015; Graham *et al.* 2019), which may be used as a direct measure of ecosystem resilience (Kéfi *et al.* 2014). Developed for image classification and computer vision, texture analysis characterizes each pixel in an image by a summary statistic of its neighboring pixels, and represents a measure of local heterogeneity which itself varies across the landscape (Haralick *et al.* 1973). Texture analysis of forested areas detects heterogeneity of overstory vegetation, which corresponds to fuel loading and continuity, capturing the primary influence of vegetation structure on fire behavior.

Remote sensing potential annual heat load

We used the digital elevation model to calculate the potential annual heat load (Supplemental Equation 5 at each pixel, which is an integrated measure of latitude, slope, and a folding transformation of aspect about the northeast-southwest line, such that northeast becomes 0 radians and southwest becomes π radians (McCune & Keon 2002; with correction in McCune 2007):

$$
\begin{aligned}
aspect_{folded} &= |\pi - |aspect - \frac{5\pi}{4}|| \\
& - 1.467 + \\
& 1.582 * cos(latitude)cos(slope) - \\
log(pahl) &= 1.5 * cos(aspect_{folded})sin(slope)sin(latitude) - \\
& 0.262 * sin(lat)sin(slope) + \\
& 0.607 * sin(aspect_{folded})sin(slope)
\end{aligned}
\tag{1}
$$

Where *pahl* is the potential annual heat load, $aspect_{folded}$ is a transformation of aspect in radians, and both *latitude* and *slope* are extracted from a digital elevation model with units of radians.

Remote sensing wildfire severity

Wildfire severity typically describes the proportion of vegetation mortality resulting from fire (Keeley 2009), and can be measured by comparing pre- and postfire satellite imagery for a specific area (Key & Benson

2006). This usually requires considerable manual effort for image collation and processing, followed by calibration with field data (Miller & Thode 2007; Miller *et al.* 2009; De Santis *et al.* 2010; Cansler & McKenzie 2012; Veraverbeke & Hook 2013; Parks *et al.* 2014; Prichard & Kennedy 2014; Edwards *et al.* 2018; Fernández-García *et al.* 2018). Herculean efforts to measure severity across broad spatial extents, such as the Monitoring Trends in Burn Severity project (Eidenshink *et al.* 2007), exist but often must sacrifice coverage of smaller fires which are far more common (Calkin *et al.* 2005), may have different severity expectations compared to larger fires (Cansler & McKenzie 2014; Harvey *et al.* 2016), and are generally important contributors to global fire effects (Randerson *et al.* 2012). Automated efforts to remotely assess wildfire have arisen, but they tend to focus on more aggregate measures of wildfire such as whether an area burned or the probability that it burned rather than the severity of the burn (Bastarrika *et al.* 2011; Goodwin & Collett 2014; Boschetti *et al.* 2015; Hawbaker *et al.* 2017), but see (Reilly *et al.* 2017; Parks *et al.* 2018). Here, we present a method to automate the measurement of wildfire severity using minimal user inputs: a geometry of interest (a wildfire perimeter or a field plot location) and an alarm date (the date the fire was discovered). This information is readily available in many fire-prone areas (such as California, via the Fire and Resource Assessment Program; http://frap.fire.ca.gov/projects/fire_data/fire_perimeters_index) or could be derived using existing products (such as the Landsat Burned Area Essential Climate Variable product described in Hawbaker *et al.* (2017)).

We calibrate 28 configurations of our algorithmic approach to ground-based wildfire severity measurements, and select the best performing severity metric to generate a comprehensive, system-wide severity dataset. Our approach more than doubles the number of fire events represented from 432 to 1008, though only increases the total burned area represented from 7.40e+05 to 8.27e+05 hectares because most of the additional fires are small.

Fetching and processing pre- and postfire imagery

For each fire perimeter, we fetched a time series of prefire Landsat images starting the day before the fire alarm date and extending backward in time by a pre-deined time window. An analogous postfire time series of Landsat imagery was fetched exactly one year after the date range used to filter the prefire collection. We tested 4 time windows, 16, 32, 48, or 64 days, which were chosen to ensure that at least 1, 2, 3, or 4 Landsat images were captured by the date range (Supplemental Fig. 1). The Landsat archive we filtered included imagery from Landsat 4, 5, 7, and 8, so each pre- and postfire image collection may contain a mix of scenes from different satellite sources to enhance coverage. For each image in the pre- and postfire image collections, we masked pixels that were not clear (i.e., clouds, cloud shadows, snow, and water) using the

CFMask algorithm (Foga *et al.* 2017).

For each Landsat image in the prefire and postfire collections, we calculated standard indices that capture vegetation cover and fire effects such as charring. Normalized difference vegetation index (NDVI) correlates with vegetation density, canopy cover, and leaf area index (Rouse *et al.* 1973). Normalized burn ratio (NBR) and normalized burn ratio version 2 (NBR2) respond strongly to fire effects on vegetation (García & Caselles 1991; Key & Benson 2006; Hawbaker *et al.* 2017; USGS 2017a, b) (Equations in Supplemental Methods).

We composited each pre- and postfire image collection (including the pixel values representing NDVI, NBR, and NBR2) into a single pre- and postfire image using a median reducer, which calculated the median of the unmasked values on a per-pixel basis across the stack of images in each collection. Composite pre- and postfire images can be successfully used to measure wildfire severity instead of using raw, individual images (Parks *et al.* 2018, 2019).

Spectral indices of wildfire severity

Using the composited images, we calculated commonly used metrics of remotely-sensed wildfire severity to validate against ground-based data: the relative burn ratio (RBR) (Parks *et al.* 2014), the delta normalized burn ratio (dNBR) (Eidenshink *et al.* 2007; Miller & Thode 2007), the relative delta normalized burn ratio (RdNBR) (Miller & Thode 2007; Miller & Safford 2012), the delta normalized burn ratio 2 (dNBR2) (Hawbaker *et al.* 2017), the relative delta normalized burn ratio 2 (RdNBR2), and the delta normalized difference vegetation index (dNDVI) (Eidenshink *et al.* 2007). We also calculated an analogous metric to RdNBR using NDVI: the relative delta normalized difference vegetation index (RdNDVI). Following Reilly *et al.* (2017), we did not correct the delta indices using a phenological offset value, as our approach implicitly accounts for phenology by incorporating multiple cloud-free images across the same time window both before the fire and one year later.

Normalized difference vegetation index (NDVI; Supplemental Equation 1) correlates with vegetation density, canopy cover, and leaf area index (Rouse *et al.* 1973). Normalized burn ratio (NBR; Supplemental Equation 3) and normalized burn ratio version 2 (NBR2; Supplemental Equation 4) respond strongly to fire effects on vegetation (García & Caselles 1991; Key & Benson 2006; Hawbaker *et al.* 2017; USGS 2017b, a).

(2) $ndvi = (nir - red)/(nir + red) * 1000$

(3) $nbr = (nir - swir2)/(nir + swir2) * 1000$

(4) $nbr2 = (swir1 - swir2)/(swir1 + swir2) * 1000$

Where *nir* is the near infrared band (band 4 on Landsat 4, 5, and 7; band 5 on Landsat 8) and *red* is the red band (band 3 on Landsat 4, 5, and 7; band 4 on Landsat 8), $swir1$ is the first short wave infrared band (band 5 on Landsat 4, 5, and 7; band 4 on Landsat 8), $swir2$ is the second short wave infrared band (band 7 on Landsat 4, 5, 7, and 8)

We calculated the delta severity indices (dNBR, dNBR2, dNDVI) by subtracting the respective postfire indices from the prefire indices (NBR, NBR2, and NDVI) without multiplying by a rescaling constant (e.g., we did not multiply the result by 1000 as in Miller & Thode (2007); Supplemental Equation 6). Following Reilly *et al.* (2017), we chose not to correct the delta indices using a phenological offset value (typically calculated as the delta index in homogeneous forest patch outside of the fire perimeter), as our approach implicitly accounts for phenology by incorporating multiple cloud-free images across the same time window both before the fire and one year later.

$$(5)\ \ dI = I_{\text{prefire}} - I_{\text{postfire}}$$

We calculated the relative delta severity indices, RdNBR and RdNDVI, by scaling the respective delta indices (dNBR and dNDVI) from Supplemental Equation 7 by a square root transformation of the absolute value of the prefire index:

$$(6)\ \ RdI = \frac{dI}{\sqrt{|I_{\text{prefire}}/1000|}}$$

We calculated the relative burn ratio (RBR) following Parks *et al.* (2014) using Supplemental Equation 8:

$$(7)\ \ RBR = \frac{dNBR}{NBR_{\text{prefire}}/1000 + 1.001}$$

Calibrating remotely-sensed wildfire severity with field-measured wildfire severity

We calibrated these 28 severity metrics with 208 field measures of fire effects to overstory vegetation— the overstory component of the Composite Burn Index (CBI)— from two previously published studies (Zhu *et al.* 2006; Sikkink *et al.* 2013). CBI is a metric of vegetation mortality across several vertical vegetation strata within a 30m diameter field plot, and the overstory component characterizes fire effects to the overstory vegetation specifically (Key & Benson 2006). CBI ranges from 0 (no fire impacts) to 3 (very high fire impacts), and has a long and successful history of use as a standard for calibrating remotely-sensed severity data in western U.S. dry forests (Key & Benson 2006; Miller & Thode 2007; Miller *et al.* 2009; Cansler & McKenzie 2012; Parks *et al.* 2014, 2018; Prichard & Kennedy 2014).

Following Miller & Thode (2007), Miller *et al.* (2009), Parks *et al.* (2014), and Parks *et al.* (2018), we fit a non-linear model to each remotely-sensed severity metric of the following form:

(8) $\text{remote\_severity} = \beta_0 + \beta_1 e^{\beta_2 \text{cbi\_overstory}}$

We fit the model in Supplemental Equation 9 for all 7 of our remotely-sensed severity metrics (RBR, dNBR, RdNBR, dNBR2, RdNBR2, dNDVI, RdNDVI) using 4 different time windows from which to collate satellite imagery (16, 32, 48, and 64 days). Following Cansler & McKenzie (2012), Parks *et al.* (2014), and Parks *et al.* (2018), we used bilinear interpolation to extract remotely-sensed severity at the locations of the CBI field plots to better align remote and field measurements. We also extracted remotely-sensed severity values using bicubic interpolation, which produces smoother imagery but is more computationally demanding. In total, we fit 56 models (7 severity measures, 4 time windows, 2 interpolation methods) and performed five-fold cross validation using the `modelr` and `purrr` packages in R (R Core Team 2018; Henry & Wickham 2019; Wickham 2019). To compare goodness of model fits with Miller & Thode (2007), Miller *et al.* (2009), and Parks *et al.* (2014), we report the average R^2 value from the cross validation for each of the 56 models.

Supplemental figures and tables

Supplemental Table 1: Comparison of models used to validate and calibrate remotely sensed wildfire severity with ground-based composite burn index (CBI) severity sorted in descending order by the R^2 value from a 10-fold cross validation. A total of 56 models were tested representing all possible combinations of 7 different measures of wildfire severity (RBR, dNBR, dNBR2, RdNBR, RdNBR2, dNDVI, and RdNDVI), 4 different time windows in which Landsat imagery was acquired and summarized with a median reducer on a pixel-by-pixel basis (16 days, 32 days, 48 days, and 64 days), and two different interpolation methods (bilinear and bicubic). The three parameters (β_0, β_1, and β_2) from the nonlinear model fit described in Eq. 1 are reported. For each model, the value of the remotely sensed wildfire severity measurement corresponding to the lower bounds of 3 commonly used categories of severity are reported ('low' corresponds to a CBI value of 0.1, 'mod' corresponds to a CBI value of 1.25, and 'high' corresponds to a CBI value of 2.25)

Rank	Severity measure	Time window	Interpolation	k-fold R^2	β_0	β_1	β_2	low	mod	high
1	RBR	48	bicubic	0.806	13.88	28.24	1.001	45.1	112.6	282.3
2	RdNBR	32	bilinear	0.802	-15.28	96.81	0.857	90.19	267.2	650.1
3	RdNDVI	32	bilinear	0.802	-80.04	100.4	0.624	26.85	138.9	328.5
4	RBR	64	bilinear	0.796	17.08	27.37	1.003	47.34	113	278.7
5	RdNDVI	48	bicubic	0.796	-82.95	114.6	0.587	38.58	155.7	346.1
6	RdNDVI	64	bicubic	0.793	-79.8	112.9	0.59	39.94	156.1	345.6
7	RdNBR	64	bilinear	0.791	-13.29	95.85	0.862	91.19	268.3	653.4
8	RdNDVI	32	bicubic	0.789	-86.56	104.6	0.619	24.74	140.3	334.7
9	RdNBR	48	bicubic	0.787	-27.14	101.8	0.852	83.7	268	664.7
10	RdNDVI	48	bilinear	0.785	-67.8	103.5	0.609	42.21	153.9	340

Rank	Severity measure	Time window	Interpolation	k-fold R^2	β_0	β_1	β_2	low	mod	high
11	RBR	32	bicubic	0.785	13.38	28.94	0.994	45.34	113.6	284
12	RdNDVI	64	bilinear	0.778	-67.67	103.9	0.607	42.77	154.2	339.3
13	RBR	32	bilinear	0.773	14.45	28.92	0.985	46.35	113.5	279.6
14	RBR	64	bicubic	0.772	15.62	27.48	1.01	46.02	112.8	282.5
15	dNDVI	32	bicubic	0.766	-57.93	72.92	0.65	19.89	106.4	257
16	RdNBR	32	bicubic	0.765	-30.17	105.6	0.841	84.72	272	670.4
17	RdNBR	16	bicubic	0.763	11.69	77.35	0.926	96.55	257.7	632.4
18	RBR	48	bilinear	0.762	17.4	27.02	1.006	47.28	112.4	277.4
19	dNDVI	32	bilinear	0.76	-52.76	69.58	0.656	21.53	105.2	251.8
20	dNBR	16	bicubic	0.76	31.67	36.21	1.058	71.92	167.6	423.1
21	dNBR	32	bilinear	0.756	29.08	36.05	1.048	69.12	162.7	409.9
22	dNBR	48	bicubic	0.753	29.81	34.55	1.069	68.25	161.3	413
23	dNDVI	64	bilinear	0.75	-46.03	74.88	0.627	33.69	117.9	261
24	RdNBR	64	bicubic	0.749	-45.8	115.5	0.819	79.53	275.7	683.4
25	RdNBR2	64	bilinear	0.746	64.09	14.28	1.204	80.2	128.4	278.3
26	RBR	16	bilinear	0.741	21.28	26.04	1.016	50.1	114	277.6
27	RBR	16	bicubic	0.741	20.64	25.8	1.028	49.24	113.9	281.4
28	dNBR	64	bicubic	0.741	33.09	32.97	1.086	69.84	161.2	412.7
29	RdNBR2	32	bicubic	0.74	45.08	18.99	1.125	66.33	122.6	283.8
30	RdNBR2	48	bilinear	0.738	56.99	15.7	1.174	74.65	125.1	277.2
31	dNDVI	48	bilinear	0.733	-43.97	72.96	0.637	33.79	117.9	262.1
32	RdNDVI	16	bicubic	0.731	-39.46	84.78	0.665	51.16	155.2	339
33	RdNBR2	48	bicubic	0.729	58.02	14.54	1.209	74.43	123.9	278.9
34	RdNBR	16	bilinear	0.728	8.831	79.63	0.909	96.04	256.7	623.8
35	dNDVI	48	bicubic	0.725	-55.06	81.08	0.613	31.15	119.4	266.9
36	dNDVI	64	bicubic	0.721	-55.2	81.59	0.609	31.51	119.5	266.1
37	dNBR2	32	bilinear	0.72	25.56	8.591	1.149	35.2	61.7	139.6
38	dNBR2	32	bicubic	0.72	25.41	8.256	1.177	34.7	61.35	142
39	dNBR	32	bicubic	0.719	27.74	36.12	1.057	67.89	163.2	417.5
40	dNBR	48	bilinear	0.718	34.76	32.84	1.076	71.33	160.9	404.8

Rank	Severity measure	Time window	Interpolation	k-fold R^2	β_0	β_1	β_2	low	mod	high
41	RdNDVI	16	bilinear	0.709	-31.08	79.15	0.678	53.61	153.5	332.5
42	RdNBR2	32	bilinear	0.705	45.37	19.76	1.1	67.42	123.5	280.2
43	dNBR	16	bilinear	0.703	32.68	36.36	1.048	73.05	167.3	416.5
44	dNBR2	48	bilinear	0.7	32.6	6.298	1.248	39.74	62.56	136.9
45	dNBR2	48	bicubic	0.698	33.08	5.838	1.284	39.72	62.15	138
46	dNBR2	64	bicubic	0.689	37.2	5.289	1.313	43.23	64.48	138.6
47	RdNBR2	64	bicubic	0.688	66.47	13.14	1.24	81.35	128.4	280.2
48	dNDVI	16	bilinear	0.671	-23.13	60.35	0.689	41.52	119.6	261.1
49	dNDVI	16	bicubic	0.659	-29.98	65.13	0.674	39.69	121.2	266.5
50	RdNBR	48	bilinear	0.658	-108.9	162.3	0.724	65.53	292	717.8
51	dNBR	64	bilinear	0.654	35.08	32.67	1.08	71.48	161.1	406.1
52	dNBR2	64	bilinear	0.639	36.14	5.641	1.283	42.55	64.17	137.2
53	RdNBR2	16	bicubic	0.638	59.17	14.77	1.198	75.83	125.2	278
54	RdNBR2	16	bilinear	0.622	60.98	14.69	1.189	77.53	125.9	274.4
55	dNBR2	16	bilinear	0.611	29.84	8.754	1.138	39.65	66.17	143.2
56	dNBR2	16	bicubic	0.562	29.49	8.601	1.156	39.15	65.95	145.3

Supplemental Table 2: Model parameter estimates for different neighborhood sizes. Values represent the mean parameter estimates with 95% credible intervals in parentheses.

Coefficient	90m x 90m neighborhood	150m x 150m neighborhood	210m x 210m neighborhood	270m x 270m neighborhood
β_0	-2.414 (-2.575, -2.258)	-2.43 (-2.589, -2.275)	-2.435 (-2.598, -2.28)	-2.444 (-2.598, -2.29)
$\beta_{\text{nbhd\_stdev\_NDVI}}$	-0.213 (-0.251, -0.174)	-0.219 (-0.259, -0.177)	-0.211 (-0.254, -0.167)	-0.202 (-0.246, -0.157)
$\beta_{\text{prefire\_NDVI}}$	1.06 (0.931, 1.192)	1.139 (1.041, 1.236)	1.143 (1.059, 1.226)	1.126 (1.052, 1.201)
β_{fm100}	-0.576 (-0.709, -0.442)	-0.573 (-0.717, -0.434)	-0.57 (-0.707, -0.438)	-0.573 (-0.715, -0.439)

Coefficient	90m x 90m neighborhood	150m x 150m neighborhood	210m x 210m neighborhood	270m x 270m neighborhood
β_{pahl}	0.246 (0.215, 0.277)	0.244 (0.213, 0.275)	0.245 (0.215, 0.276)	0.246 (0.216, 0.277)
$\beta_{\text{topographic\_roughness}}$	0.002 (-0.029, 0.034)	0.007 (-0.026, 0.039)	0.01 (-0.022, 0.043)	0.011 (-0.023, 0.046)
$\beta_{\text{nbhd\_mean\_NDVI}}$	-0.168 (-0.311, -0.028)	-0.289 (-0.398, -0.182)	-0.308 (-0.406, -0.21)	-0.298 (-0.388, -0.207)
$\beta_{\text{nbhd\_stdev\_NDVI*prefire\_NDVI}}$	0.128 (0.031, 0.221)	0.062 (-0.011, 0.135)	0.028 (-0.037, 0.092)	0.016 (-0.045, 0.078)
$\beta_{\text{nbhd\_stdev\_NDVI*nbhd\_mean\_NDVI}}$	-0.115 (-0.206, -0.022)	-0.057 (-0.13, 0.014)	-0.012 (-0.074, 0.05)	0.01 (-0.048, 0.068)
$\beta_{\text{nbhd\_stdev\_NDVI*fm100}}$	-0.032 (-0.073, 0.01)	-0.028 (-0.072, 0.016)	-0.02 (-0.065, 0.024)	-0.01 (-0.056, 0.036)
$\beta_{\text{nbhd\_mean\_NDVI*prefire\_NDVI}}$	-0.54 (-0.587, -0.494)	-0.53 (-0.577, -0.483)	-0.517 (-0.565, -0.47)	-0.505 (-0.552, -0.458)

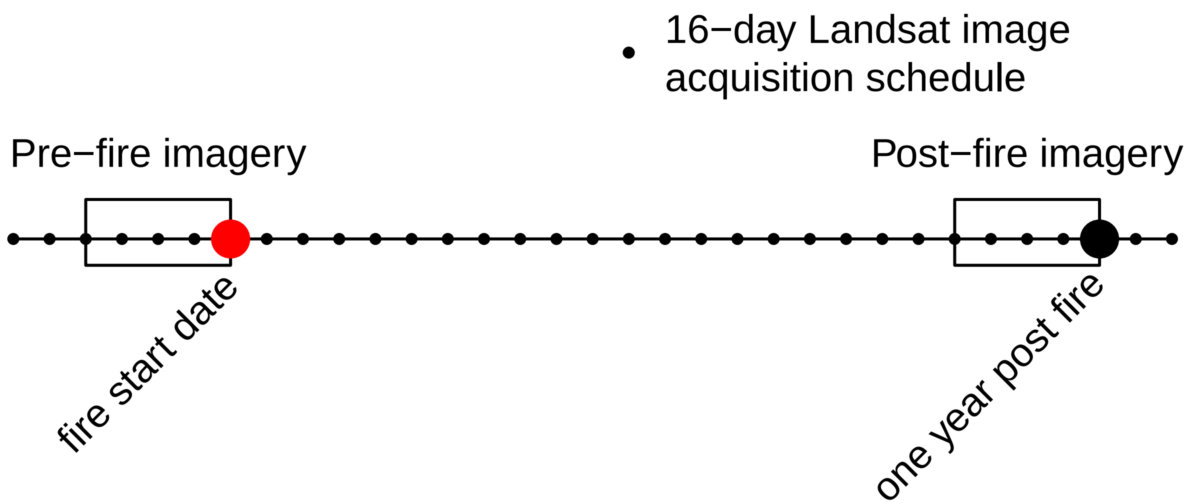

Supplemental Figure 1: Schematic for how Landsat imagery was assembled in order to make comparisons between pre- and post-fire conditions. This schematic depicts a 64-day window of image collation prior to the fire which comprise the pre-fire image collection. A similar, 64-day window collection of imagery is assembled one year after the pre-fire image collection.

References

1.

Asner, G.P., Brodrick, P.G., Anderson, C.B., Vaughn, N., Knapp, D.E. & Martin, R.E. (2016). Progressive forest canopy water loss during the 2012-2015 California drought. *Proceedings of the National Academy of Sciences*, 113, E249–E255.

2.

Bastarrika, A., Chuvieco, E. & Martín, M.P. (2011). Mapping burned areas from Landsat TM/ETM+ data with a two-phase algorithm: Balancing omission and commission errors. *Remote Sensing of Environment*, 115, 1003–1012.

3.

Boschetti, L., Roy, D.P., Justice, C.O. & Humber, M.L. (2015). MODISLandsat fusion for large area 30m burned area mapping. *Remote Sensing of Environment*, 161, 27–42.

4.

Calkin, D.E., Gebert, K.M., Jones, J.G. & Neilson, R.P. (2005). Forest Service large fire area burned and suppression expenditure trends, 19702002. *j for*, 103, 179–183.

5.

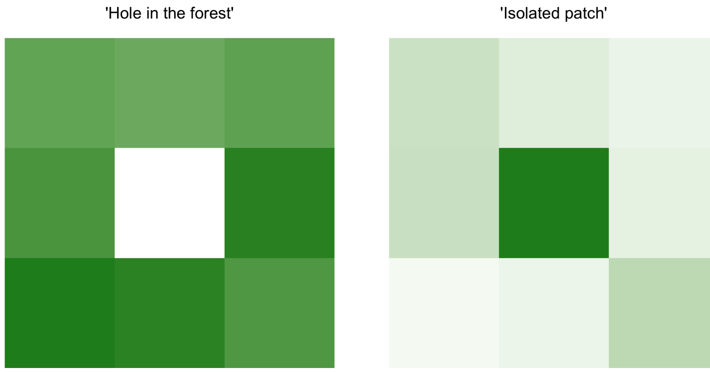

Supplemental Figure 2: Conceptual diagram of 'decoupling' that sometimes occurs between the central pixel NDVI and the neighborhood mean NDVI. In each of these scenarios, our model results suggest that the probability that the central pixel burns at high severity is higher than expected given the additive effect of the covariates. The left panel depicts the "hole in the forest" decoupling, which occurs more frequently, and the right panel depicts the "isolated patch" decoupling.

Cansler, C.A. & McKenzie, D. (2012). How robust are burn severity indices when applied in a new region? Evaluation of alternate field-based and remote-sensing methods. *Remote Sensing*, 4, 456–483.

6.

Cansler, C.A. & McKenzie, D. (2014). Climate, fire size, and biophysical setting control fire severity and spatial pattern in the northern Cascade Range, USA. *Ecological Applications*, 24, 1037–1056.

7.

De Santis, A., Asner, G.P., Vaughan, P.J. & Knapp, D.E. (2010). Mapping burn severity and burning efficiency in California using simulation models and Landsat imagery. *Remote Sensing of Environment*, 114, 1535–1545.

8.

Edwards, A.C., Russell-Smith, J. & Maier, S.W. (2018). A comparison and validation of satellite-derived fire severity mapping techniques in fire prone north Australian savannas: Extreme fires and tree stem mortality. *Remote Sensing of Environment*, 206, 287–299.

9.

Eidenshink, J., Schwind, B., Brewer, K., Zhu, Z.-L., Quayle, B. & Howard, S. (2007). A project for monitoring trends in burn severity. *Fire Ecology*, 3, 3–21.

10.

Fernández-García, V., Santamarta, M., Fernández-Manso, A., Quintano, C., Marcos, E. & Calvo, L. (2018). Burn severity metrics in fire-prone pine ecosystems along a climatic gradient using Landsat imagery. *Remote*

Sensing of Environment, 206, 205–217.

11.

Foga, S., Scaramuzza, P.L., Guo, S., Zhu, Z., Dilley, R.D. & Beckmann, T. *et al.* (2017). Cloud detection algorithm comparison and validation for operational Landsat data products. *Remote Sensing of Environment*, 194, 379–390.

12.

García, M.L. & Caselles, V. (1991). Mapping burns and natural reforestation using thematic Mapper data. *Geocarto International*, 6, 31–37.

13.

Goodwin, N.R. & Collett, L.J. (2014). Development of an automated method for mapping fire history captured in Landsat TM and ETM+ time series across Queensland, Australia. *Remote Sensing of Environment*, 148, 206–221.

14.

Graham, L.J., Spake, R., Gillings, S., Watts, K. & Eigenbrod, F. (2019). Incorporating fine-scale environmental heterogeneity into broad-extent models. *Methods in Ecology and Evolution*, 10, 767–778.

15.

Haralick, R.M., Shanmugam, K. & Dinstein, I. (1973). Textural features for image classification. *IEEE Transactions on Systems, Man, and Cybernetics*, SMC-3, 610–621.

16.

Harvey, B.J., Donato, D.C. & Turner, M.G. (2016). Drivers and trends in landscape patterns of stand-replacing fire in forests of the US Northern Rocky Mountains (1984-2010). *Landscape Ecology*, 31, 2367–2383.

17.

Hawbaker, T.J., Vanderhoof, M.K., Beal, Y.-J., Takacs, J.D., Schmidt, G.L. & Falgout, J.T. *et al.* (2017). Mapping burned areas using dense time-series of Landsat data. *Remote Sensing of Environment*, 198, 504–522.

18.

Henry, L. & Wickham, H. (2019). *Purrr: Functional programming tools.*

19.

Huang, Q., Swatantran, A., Dubayah, R. & Goetz, S.J. (2014). The influence of vegetation height heterogeneity on forest and woodland bird species richness across the United States. *PLoS ONE*, 9, e103236.

20.

Keeley, J.E. (2009). Fire intensity, fire severity and burn severity: A brief review and suggested usage. *International Journal of Wildland Fire*, 18, 116.

21.

Key, C.H. & Benson, N.C. (2006). Landscape assessment (LA): Sampling and analysis methods, 55.

22.

Kéfi, S., Guttal, V., Brock, W.A., Carpenter, S.R., Ellison, A.M. & Livina, V.N. *et al.* (2014). Early warning signals of ecological transitions: Methods for spatial patterns. *PLoS ONE*, 9, e92097.

23.

McCune, B. (2007). Improved estimates of incident radiation and heat load using non- parametric regression against topographic variables. *Journal of Vegetation Science*, 18, 751–754.

24.

McCune, B. & Keon, D. (2002). Equations for potential annual direct incident radiation and heat load. *Journal of Vegetation Science*, 13, 603–606.

25.

Miller, J.D., Knapp, E.E., Key, C.H., Skinner, C.N., Isbell, C.J. & Creasy, R.M. *et al.* (2009). Calibration and validation of the relative differenced Normalized Burn Ratio (RdNBR) to three measures of fire severity in the Sierra Nevada and Klamath Mountains, California, USA. *Remote Sensing of Environment*, 113, 645–656.

26.

Miller, J.D. & Safford, H. (2012). Trends in wildfire severity: 1984 to 2010 in the Sierra Nevada, Modoc Plateau, and Southern Cascades, California, U.S.A. *Fire Ecology*, 8, 41–57.

27.

Miller, J.D. & Thode, A.E. (2007). Quantifying burn severity in a heterogeneous landscape with a relative version of the delta Normalized Burn Ratio (dNBR). *Remote Sensing of Environment*, 109, 66–80.

28.

Parks, S.A., Holsinger, L.M., Koontz, M.J., Collins, L., Whitman, E. & Parisien, M.-A. *et al.* (2019). Giving ecological meaning to satellite-derived fire severity metrics across North American forests. *Remote Sensing*, 11, 1735.

29.

Parks, S.A., Holsinger, L.M., Panunto, M.H., Jolly, W.M., Dobrowski, S.Z. & Dillon, G.K. (2018). High-severity fire: Evaluating its key drivers and mapping its probability across western U.S. Forests. *Environmental*

Research Letters, 13, 044037.

30.

Parks, S., Dillon, G. & Miller, C. (2014). A new metric for quantifying burn severity: The Relativized Burn Ratio. *Remote Sensing*, 6, 1827–1844.

31.

Prichard, S.J. & Kennedy, M.C. (2014). Fuel treatments and landform modify landscape patterns of burn severity in an extreme fire event. *Ecological Applications*, 24, 571–590.

32.

Randerson, J.T., Chen, Y., Werf, G.R. van der, Rogers, B.M. & Morton, D.C. (2012). Global burned area and biomass burning emissions from small fires. *Journal of Geophysical Research: Biogeosciences*, 117.

33.

R Core Team. (2018). *R: A language and environment for statistical computing.* R Foundation for Statistical Computing, Vienna, Austria.

34.

Reilly, M.J., Dunn, C.J., Meigs, G.W., Spies, T.A., Kennedy, R.E. & Bailey, J.D. *et al.* (2017). Contemporary patterns of fire extent and severity in forests of the Pacific Northwest, USA (1985-2010). *Ecosphere*, 8, e01695.

35.

Rouse, W., Haas, R.H., Deering, W. & Schell, J.A. (1973). *Monitoring the vernal advancement and retrogradation (green wave effect) of natural vegetation* (Type II Report No. RSC 1978-2). Goddard Space Flight Center, Greenbelt, MD, USA.

36.

Sikkink, P.G., Dillon, G.K., Keane, R.E., Morgan, P., Karau, E.C. & Holden, Z.A. *et al.* (2013). Composite Burn Index (CBI) data and field photos collected for the FIRESEV project, western United States.

37.

Stein, A., Gerstner, K. & Kreft, H. (2014). Environmental heterogeneity as a universal driver of species richness across taxa, biomes and spatial scales. *Ecology Letters*, 17, 866–880.

38.

Tuanmu, M.-N. & Jetz, W. (2015). A global, remote sensing-based characterization of terrestrial habitat heterogeneity for biodiversity and ecosystem modelling: Global habitat heterogeneity. *Global Ecology and Biogeography*, 24, 1329–1339.

39.

USGS. (2017a). Landsat 4-7 Surface Reflectance (LEDAPS) Product Guide, 41.

40.

USGS. (2017b). Landsat 8 Surface Reflectance Code (LASRC) Product Guide, 40.

41.

Veraverbeke, S. & Hook, S.J. (2013). Evaluating spectral indices and spectral mixture analysis for assessing fire severity, combustion completeness and carbon emissions. *International Journal of Wildland Fire*, 22, 707.

42.

Wickham, H. (2019). *Modelr: Modelling functions that work with the pipe.*

43.

Wood, E.M., Pidgeon, A.M., Radeloff, V.C. & Keuler, N.S. (2012). Image texture as a remotely sensed measure of vegetation structure. *Remote Sensing of Environment*, 121, 516–526.

44.

Young, D.J.N., Stevens, J.T., Earles, J.M., Moore, J., Ellis, A. & Jirka, A.L. *et al.* (2017). Long-term climate and competition explain forest mortality patterns under extreme drought. *Ecology Letters*, 20, 78–86.

45.

Zhu, Z., Key, C., Ohlen, D. & Benson, N. (2006). *Evaluate sensitivities of burn-severity mapping algorithms for different ecosystems and fire histories in the United States* (Final Report to the Joint Fire Science Program No. JFSP 01-1-4-12).